PAPER

Fingerprints of short-range and long-range structure in BaZr$_{1-x}$Hf$_x$O$_3$ solid solutions: an experimental and theoretical study†

Rafael Uarth Fassbender,[a] Tatiane Strelow Lilge,[a] Sergio Cava,[b] Juan Andrés,[c] Luis Fernando da Silva,[d] Valmor Roberto Mastelaro,[d] Elson Longo[e] and Mario Lucio Moreira*[a]

A microwave-assisted hydrothermal method was applied to synthesize BaZr$_{1-x}$Hf$_x$O$_3$, (BZHO) solid solutions at a low temperature, 140 °C, and relatively short times, 160 min. The detailed features of the crystal structure, at both short and long ranges, as well as the crystal chemistry doping process, are extensively analysed. X-ray diffraction measurements and Raman spectroscopy have been used to confirm that pure and Hf-doped BZO materials present a cubic structure. Extended X-ray absorption fine structure (EXAFS) spectra indicate that Hf^{4+} ions have replaced the Zr^{4+} ions on the 6-fold coordination and a subsequent change on the Ba^{2+} 12-fold coordination can be sensed. X-ray absorption near-edge structure (XANES) spectroscopy measurements reveal a local symmetry breaking process, associated to overlap of the 4d–2p and 5d–2p orbitals of Zr–O and Hf–O bonds, respectively. Field emission scanning electron microscopy (FE-SEM) and high resolution transmission electron microscopy (HRTEM) show the mesocrystalline nature of self-assembled BZHO nanoparticles under a dodecahedron shape. In addition first principle calculations were performed to complement the experimental data. The analysis of the band structures and density of states of the undoped BZO and doped BZHO host lattice allow deep insight into the main electronic features. The theoretical results help us to find a correlation between simulated and experimental Raman modes and allow a more substantial interpretation of crystal structure.

1 Introduction

Modern scientific research is constantly looking for innovative ideas and it could not be different for highly promising systems such as perovskite based materials.[1–3]

As a typical perovskite material, barium zirconate (BaZrO$_3$, BZO) is of both fundamental interest and practical importance in many applications. This material is chemically and thermally stable,[4,5] including their optical properties which were observed under different circumstances, from quasi-amorphous compounds[6] through quasi-crystalline systems[6,7] and finally to periodic crystals.[8,9] BZO presents a cubic perovskite symmetry with ZrO$_6$ octahedral and BaO$_{12}$ cubooctahedral clusters. All individual or conjugated clusters contributing to both electronic and optical properties such as a high dielectric constant and a reasonable wide band-gap around ∼5.4 eV,[10] which are important properties for energy related applications. In particular, these properties have made possible the application of BZO as superconductor pinning centers[11,12] to improve the typical superconductive features. Recently, Borja-Urby *et al.*, reported the photocatalytic activity for pure BZO and Bi doped BZO. In both cases the photocatalyst efficiency depends strongly on Bi content as well as induced defects.[13] Recently, we have reported first order Raman modes for a BZO system synthesized by a microwave-assisted hydrothermal (MAH)[7] method assigned to local disorder, which are responsible for its emergent optical features. In addition, other optical properties have been discovered such as the conversion of ionizing radiation into visible light for BZO obtained by the same methodology.[14]

[a] CCAF, Instituto de Física e Matemática (IFM), Departamento de Física, Universidade Federal de Pelotas, Campus do Capão do Leão, Caixa Postal, 354, CEP 96010-970, Pelotas, RS, Brazil. E-mail: mlucio3001@gmail.com; Fax: +55 53 3275-7614; Tel: +55 53 3275-7614

[b] CCAF, Graduate Program in Science and Materials Engineering, Technology Development Center, Federal University of Pelotas, 96010-900 Pelotas, RS, Brazil

[c] Departament de Química Física i Analítica, Universitat Jaume I, Campus de Riu Sec, Castelló E-12080, Spain

[d] Instituto de Física de São Carlos, USP, PO Box 369, 13560-970 São Carlos, SP, Brazil

[e] INCTMN, Department of Physical Chemistry, Institute of Chemistry, Unesp - Universidade Estadual Paulista, Prof. Francisco Degni Street, s/nº, Quitandinha, Araraquara, SP, 14800-900, Brazil

† Electronic supplementary information (ESI) available. See DOI: 10.1039/c4cp05448b

This journal is © the Owner Societies 2015

Phys. Chem. Chem. Phys., 2015, **17**, 11341–11349 | **11341**

The exploration of optical transitions covers a broad range of luminescent applications of perovskite based materials, increasing the interest and design of these functional materials. Introducing a small amount of foreign elements (usually transition metals or rare-earth elements)[15] into the conventional metal oxide or to make a solid ternary solid solution, which can display compositionally tunable properties, are well known strategies used to manipulate the band gap value.[16] The dopant's may generate new energy levels between the valence band (BV) and conduction band (CB) of the metal oxide resulting in a reduced minimum light absorption energy gap of the host lattice. This process is capable to tailor the electronic structures by establishing new energy bands or localized impurity levels into the band gaps, and thus to extend the light-response range. Then, it is the key for the appearance of new properties and the potential applications have pushed forward increasing demands of more systematic and profound understanding on, say, crystalline structures and transformations among the polymorphous, defect and coordination chemistry, symmetries of local environments surrounding dopant's and so on.

The MAH method has demonstrated its efficiency in the synthesis of materials with new and/or intensified properties.[17–21] The advantages of this synthesis method are the strong reduction in time and temperatures even compared with hydrothermal and/or solvothermal conventional methodologies.[22,23] Another relevant aspect is the microwave radiation action producing, besides the temperature increase, but also a rise in the ionic conduction, charge polarization and possible hot spots throughout the solution.[24,25] All these intrinsic features of microwave heating are able to be responsible for local and/or periodic distortions, together or separately. In this respect, we present the first study of the effects of Hf-doping on the BZO material, by using the MAH method, to obtain $BaZr_{1-x}Hf_xO_3$, $x = 0.01, 0.02, 0.04, 0.08$ and 0.16, (BZHO) solid solutions. To truly understand the both short and large-range structures, different experimental techniques as well as first principle calculations have been carried out. The results are correlated with two techniques probing the local features of structure and bonding, $i.e.$, X-ray absorption near-edge structure (EXAFS) spectroscopy and Raman spectroscopy.[26] These techniques complement X-ray diffraction (XRD) measurements. The XANES spectroscopy is able to determine the chemical surrounding ($e.g.$, crystal field, density of unoccupied states, and the orientation of the specimen with respect to the polarization of the photon).[27,28] Typically, measurements are made in transmission mode if attenuation length of the photon in the material being analysed is sufficiently long; however, in the soft X-ray region, due to small attenuation length, XANES measurements are made by detecting total electron yield (TEY), which is surface sensitive.[29] In the case of BZHO the absorptions of Zr K-edge and Hf L_{III}-edge can be obtained by XANES/EXAFS transmission mode, while for Ba L_{III}-edge and Zr L_{III}/L_{II}-edge the TEY methodology is more appropriated to operating conditions of the National Synchrotron Light Laboratory (LNLS). The X-ray absorption spectroscopy (XAS) has been applied in many case to investigate the local distortions of the BZO perovskite.[26,30] On the other hand, Raman spectroscopy is able to investigate the polarizations of both asymmetric and symmetric bonds in the crystal,[31]

and first-order vibrational modes can be used to study local distortions.[26]

2 Methods and model systems

MAH method $i.e.$ hydrothermal synthesis under microwave radiation was developed as follows: firstly the concentrations of Hf atom were chosen obeying the "2^n" model, where "n" is the ordinal number and the result corresponds to the Hf atom concentration. Then, with $n = 0$ the Hf concentration is 1%, with $n = 1$ is 2%, and so on. All precursors were metal chlorides and have the analytical grade in the order of 99%. Each precursor was diluted in double deionized water under constant stirring at 50 °C to avoid and/or prevent carbonate formations. The molar concentrations of the host matrix is 0.01054 mol L^{-1} for Ba and Zr atoms, being the Hf concentration a molar percentage of Zr with $n = 0, 1, 2, 3$ and 4. After mixing, the precursors were co-precipitated by KOH at 6 mol L^{-1} and immediately transferred to a closed 110 mL polytetrafluoroethylene vessel and placed into a microwave system.

The microwave system applies 2.45 GHz of radiation (ESI,† S1) with a maximum output power of 800 W. The reaction mixture was heated to 140 °C in less than 1 min (at 800 W) by a direct interaction between water molecules and microwave radiation, maintaining this temperature for 160 (BZO160) min under a pressure of 2.5 Bar. After the microwave annealing the final white powders were washed with double deionized water until pH = 7 and was finalized by absolute ethanol straining. The powders were dried at 80 °C over night (around 12 h) in a stove.

Several experimental characterization techniques were carried out, such as X-ray diffraction by Rigaku DMax 2500PC using Cu $K_{\alpha1}$ ($\lambda = 1.5406$ Å) and Cu $K_{\alpha2}$ ($\lambda = 1.54434$ Å) radiation. The Raman spectra were recorded on a RFS/100/S Bruker Fourier transform Raman (FT-Raman) spectrometer with a Nd:YAG laser providing an excitation light at 1064 nm in a spectral resolution of 4 cm^{-1} and keeping its maximum output power at 85 mW. To analyse the morphology and crystal growth orientation a scanning electron microscope Zeiss VP Supra 35 equipped with a field emission gun (FE-SEM) and a high resolution transmission electron microscope (TEM) Philips CM200, 200 kV with microanalysis were used. For XANES, the Zirconium K and L_{III}-edge X-ray absorption was chosend and the spectra were collected at the LNLS (National Synchrotron Light Laboratory) facility using the D04B-XAFSII and D04A-SXS beam lines, respectively. The LNLS storage ring was operated at 1.36 GeV and 160 mA. The Zirconium K-edge XANES and EXAFS spectra were collected in transmission mode at room temperature while in the soft X-ray region, due to small attenuation length, the Zr L_{III}-edge XANES measurements were made by detecting the total electron yield (TEY), which is surface sensitive. UV-visible absorption was recorded using the Cary 5G spectrometer in total reflection mode by the integration sphere in the region of 200 to 800 nm. All measurements were taken at room temperature.

The periodic density functional theory (DFT) method, applying the B3LYP functional[32–34] to take into account both exchange

11342 | $Phys. Chem. Chem. Phys.$, 2015, **17**, 11341–11349

This journal is © the Owner Societies 2015

and correlations integration, has already been successfully employed[35,36] by using the CRYSTAL06 package code.[37] To control the accuracy, the Coulomb and exchange integrals were set to 10^{-8} (ITOL1 to ITOL4) and 10^{-14} (ITOL5), whereas the percentage of Fock–Kohn–Sham matrix mixing was set to 40 (IPMIX = 40). The reciprocal space was generated according to a regular sub-lattice determined by the shrinking factor which was set to 6 (13–20 independent k-points in the irreducible part of the Brillouin zone).[37] This methodology is well recognized by its performance to simulate electronic and geometric properties of materials with significant accuracy. The atomic centers have been described by all electron basis sets for Ba and Zr atoms (available from http://www.tcm.phy.cam.ac.uk/mdt26/crystal.html) and 6-31G* for O atom.

Initially, an optimization of the lattice parameter has been performed, from this optimized structure, a $2 \times 2 \times 2$ supercell was constructed to represent a doped superstructure with a specific content of Hf atoms. To construct the supercell, a model of imperfect crystals of cubic primitive (P) cell[38] was employed. In our case one Zr atom was placed into the supercell resulting in 12.5% of Hf atom in the BZO host lattice. It should be emphasized that the amount of Hf is based on previous semi-quantitative microanalysis results of our samples (to be addressed later). The accuracy factor was the same described previously always aiming for the total energy minimization. After the simulation the band structure and density of states were obtained using the ANA package code.

3 Results and discussion

3.1 X-ray and Raman

As it was commented, a staggered bottom-up structure was made-up by the BZO host matrix doped with Hf under concentrations of 1, 2, 4, 8 and 16%, obeying the kinetic model 2^n, being n = 0, 1, 2, 3 and 4. The powder diffraction patterns can be analysed from the Fig. 1, the absence of a significant amount
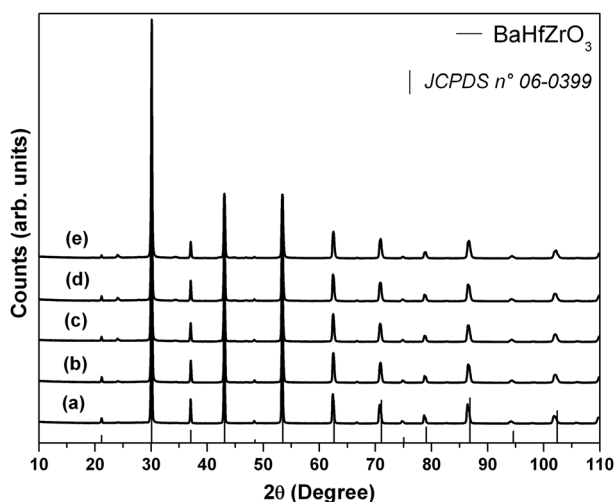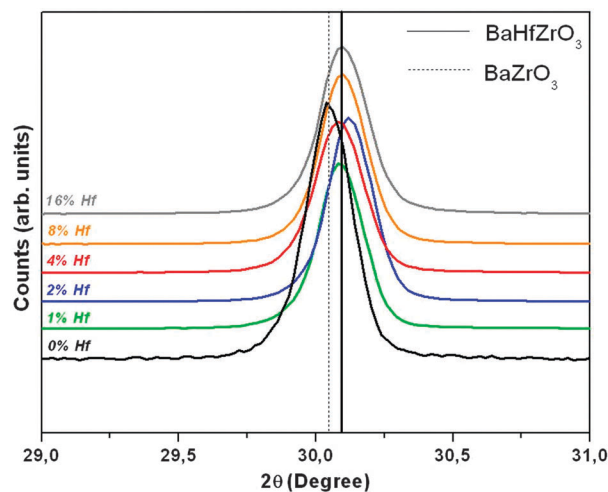

Fig. 2 Magnification of main diffraction peak (110), evidencing the displacement between pure BZO and BHZO doped with hafnium.

of secondary phases is easily noted, even for higher Hf concentration. For samples doped with 4, 8 and 16%, a very weak peak at $2\theta = 24°$ associated with the most intense diffraction of the witherite phase (barium Carbonate) can be observed, however any Hf secondary phases were detected. This indicates that even a large concentration as 16%, Hf can be considered as soluble into the BZO lattice since there is no phase segregation of hafnium compounds. In addition, substantial changes in the BZO diffraction pattern assigned with the $Pm\bar{3}m$ space group as a cubic structure, are not sensed. The main peak evidenced in the Fig. 2 show a small displacement at high angles, moreover this behaviour indicates distortions in the host lattice.

An analysis of the X-ray diffraction patterns denotes that it is not capable to determinate if the Hf content was well introduced into the BZO lattice because of the absence of perceptible changes in the diffraction pattern. Then, it is mandatory to use an analytical approach associated to different spectroscopy to determine the real concentration of Hf in each case.

For pure BZO or doped BZHO, any first order Raman spectrum is expected at room temperature because of all atoms in its structure occupying sites with inversion symmetry, and it, indeed, showed by X-ray patterns corresponds to the $Pm3m$ space group. The cubic paraelectric phase allows 12 optical modes ($3F_{1u} + 1F_{2u}$) that are not Raman active.[39] Meanwhile, the Raman spectrum of BZO and BHZO showed weak bands (at 277, 352, 462, 644, 707, 739, 846 and 1016 cm^{-1}). A slight local distortion of the oxygen octahedra can result in the breakdown of Raman selection rules, thereby giving rise to weak bands in the Raman spectrum associated to slight changes in the host lattice, in agreement with the previous reports.[31,40] To this end, the measured samples with and without Hf contents were further analysed of differences among them. Raman active modes can be viewed in Fig. 3, in which even small amounts of Hf yield substantial changes for all peaks compared with pure BZO spectrum. It is important to emphasize that the crystal symmetry of BZO and BZHO samples continue to be cubic and do not measure any active Raman modes if the symmetry is kept perfect, or at least almost perfect. Thus, all actives Raman
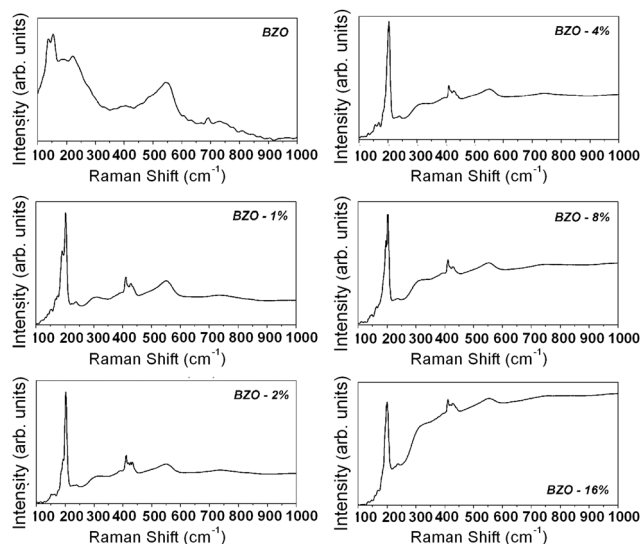

Fig. 1 X-ray diffraction of pure BZO and BZO doped with (a) 0%, (b) 1%, (c) 2%, (d) 4%, (e) 8% and (f) 16% of hafnium.

This journal is © the Owner Societies 2015

Phys. Chem. Chem. Phys., 2015, 17, 11341–11349 | 11343

Fig. 3 Room temperature Raman spectroscopy for BZO samples with hafnium under concentrations from 0 to 16%.

modes must be associated to lattice imperfections, *i.e.* distortions of the ideal structure at short-range.

An analysis of the results depicted in Fig. 3 renders that pure BZO has active modes and the values of each active vibrational mode are listed in the Table 1. The results point out that the main changes of calculated data correspond to the vibrations of the dopant site, just as a result of the replacement of Zr by Hf. Hafnium does not change the lattice symmetry as a whole but it does locally, *i.e.* change the short-range structure as it can be sensed by both theoretical and experimental values.

The activation of Raman transverse (TO) and longitudinal (LO) modes suggests that the concentration of these point defects is significantly higher than in samples prepared by other synthesis methods, in which active Raman modes were not observed. To better understand the origin of these vibrations, assigning the bands

Table 1 Theoretical (Theo) and experimental Raman modes for BZO and BHZO associated to its specific vibrations

BZO Experimental	BHZO	BZO Theoretical	BHZO	Vibration
—	—	101 (F2G) (B)	103 (F2G) (B)	Ba–O
129	—	116 (F2G) (B)	120 (F2G) (B)	Ba–O
152	162	159 (EG) (S)	161 (EG) (S)	Ba–O
191	198	195 (AG) (B)	189 (AG) (S)	Ba–O
225	241	—	—	
—	319	329 (F2G) (B)	329 (F2G) (B)	Ba–O
—	334	—	333 (F1G) (B)	Ba–O
337	—	338 (F2G) (B)	338 (F2G) (B)	O
396	393	—	—	
—	409	—	—	
457	433	—	—	
490	492	494 (F2G) (B)	492 (F2G) (B)	Ba–O
549	554	553 (F2G) (B)	551 (F2G) (B)	Zr–O, Hf–O
—	—	638 (EG) (S)	631 (EG) (S)	O
688	—	644 (BG) (S)	645 (EG) (S)	O
736	744	757 (AG) (S)	730 (AG) (S)	Ba–O
—	—	861 (EG) (S)	857 (EG) (S)	Ba–O
—	—	—	901 (AG) (S)	
—	—	920 (EG) (S)	920 (EG) (S)	Ba–O

where they belong and what kind of vibration, it is necessary to simulate these Raman modes. We have used DFT through of B3LYP functional. For pure BZO, an analysis of the results indicates that the experimental modes located around 129, 191 cm^{-1} can be related to molecular vibrations of transverse TO modes, while the modes located at 457 and 549 cm^{-1} are attributed to longitudinal and transverse vibrations, respectively, which can be considered as the first order. Besides these modes, more one second-order experimental vibrational modes located at 225 cm^{-1} were observed.[41] Supplementing the set of vibrations identified for the pure BZO spectrum of still observed modes related to barium carbonate in 153 and 695 cm^{-1}. For BZHO the experimental vibration 195 cm^{-1} was observed a little displaced in relation to 191 cm^{-1} for pure BZO. On the other hand the vibrations at 129 cm^{-1} are absent for doped samples. This modes still belongs to TO vibrations but the displacement and absence are a result of the introduction of Hf in the host lattice. The same behaviour can be observed of vibrations located at 433 cm^{-1} and 554 cm^{-1} for BZHO. Besides the second-order vibration was also displaced and for BZHO is located at 241 cm^{-1}. The Raman spectra for the BZHO can be simulated, individually analysed and compared with that obtained for the pure BZO using Table 1.

The simulated vibrational modes are in good agreement with the experimental results, although there are some modes not foreseen theoretically and some predicted modes that could not be observed. This fact is due to the fact that simulation takes into account only the primitive form of the structure as it was introduced, neglecting possible structural distortions not included in this model.

There are almost four vibrational modes that should be highlighted, being two stretching modes located around 159 and 192 cm^{-1} and two bending modes at 494 and 551 cm^{-1}. These modes appear in both structures and are not significantly modified by the introduction of Hf. Moreover modes located around 300 cm^{-1} are strongly affected causing two nearby frequencies to be present, one only in the pure sample and another one in the BZHO sample. Changes in the crystal field incorporated by Hf content leads to a bending mode at 334 cm^{-1} on the Ba–O vibration. However the effective participation of Hf is only detected by the simulations for the mode located at 333 cm^{-1}.

3.2 Theoretical model, band structure and density of states

The calculated total and the partial density of states (DOS) are depicted in Fig. 4 and 5, which reports the slight contribution of 5d orbitals of Hf to the CB region. To incorporate the Hf content into the BZO host lattice, the supercells ($2 \times 2 \times 2$) were built as shown in Fig. 6A. The simulated Hf content was 12.5%, matching the high experimental concentration. In this case the DOS intensity of Hf was intensified ten times to the better represent its 5d states contribution. A detailed analysis for the Fig. 4 and 5 renders that the modification over the relative intensity of total DOS at CB above 6 eV, can be associated to the superposition of 4d (Zr) and 5d (Hf) states. Significant changes can be sensed in the oxygen 2p region, related to the interactions
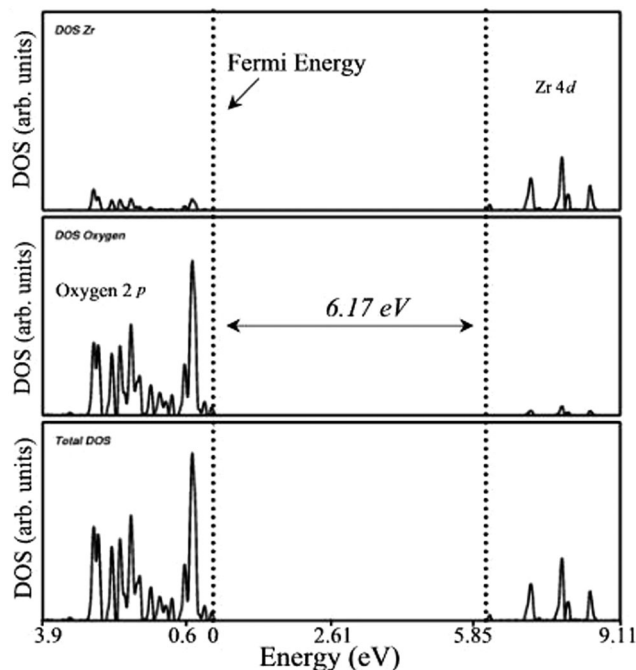
11344 | *Phys. Chem. Chem. Phys.*, 2015, **17**, 11341–11349

This journal is © the Owner Societies 2015

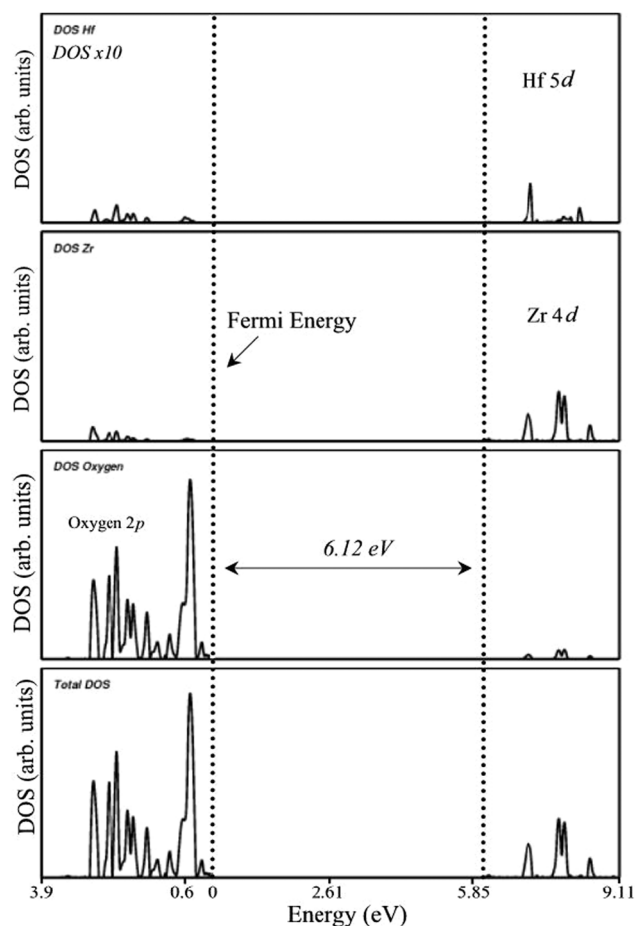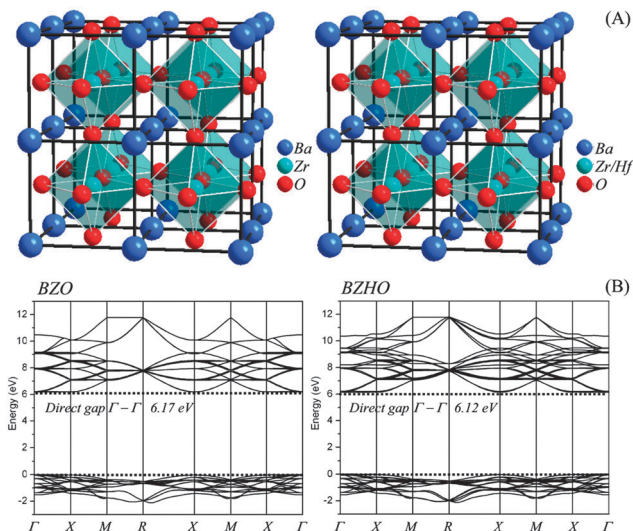**Fig. 4** Projected density of states of zirconium, oxygen and total DOS for pure BZO sample.

Fig. 6 (A) Schematic 3D cubic structure evidencing the octahedral sites for zirconium and hafnium for pure and doped samples. (B) The band structure denoting the top of the valence band and bottom of the conduction band for pure and hafnium-doped BZO.

Fig. 5 Projected density of states of hafnium ($\times$10), zirconium, oxygen and total DOS for BHZO sample.

of electronic density of states of hafnium 5d and oxygen 2p, which only can be noted by means of the convolution of the XAS techniques. From the CB for all projections, the low intensity of the projections just above the band gap leads to an idea that the gap is even greater, however projections in this region are not observed only due to its low contribution, but it does not nonexistent.

The calculated energy band structure of cubic BZO and BZHO samples along the high-symmetry points of the Brillouin (see Fig. 6B) supply arguments to discuss the host BZO lattice polarizations as Hf was added. For both situations the top of the VB is taken as the zero of energy jointly with the Fermi level. BZHO band structure corresponds to the 12.5% Hf content in the BZO system, as it is depicted in Fig. 6B. A careful inspection over the BZHO band structure shows clearly the introduction of states at the CB located above 6 eV, although in the VB the distribution changes are almost undetected.

The slight scroll down energy on the CB states can be explained as the superposition between 4d and 5d states of Zr and Hf atoms, respectively. In this case the 5d states are located at lower energies than those corresponding to Zr, leading to a slight decrease in the calculated band gap from 6.17 to 6.12 eV. This band gap originates from a transition from O 2p filled electron states located at the top of the VB to the mixed empty Zr 4d and Hf 5d electron states dominating the bottom of the CB. Previous calculations showed the direct band gap of $BaHfO_3$ is around 3 eV.[42]

3.3 X ray absorption near-edge spectroscopy

To support the results obtained from theoretical simulations, XANES was used as will be reported hereafter. Firstly, it is necessary to confirm if Hf is replacing Zr and/or Ba in the BZO lattice. Zirconium K and L_{III}-edge spectra shown in Fig. 7, 8 and
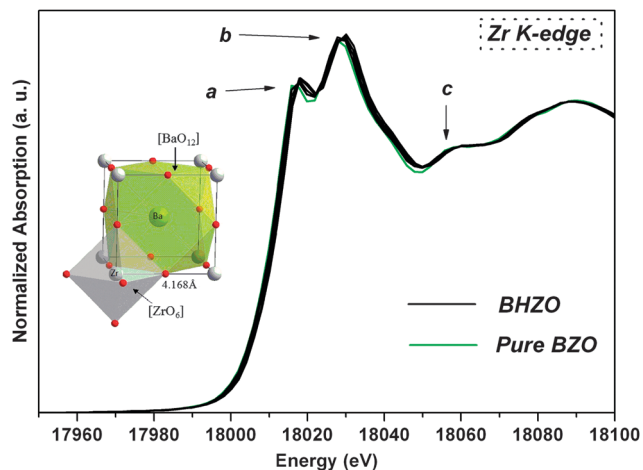
Fig. 7 Zirconium K-edge for BHZO and pure BZO showing "a", "b" and "c" peaks where the main differences are among the pure and doped samples.
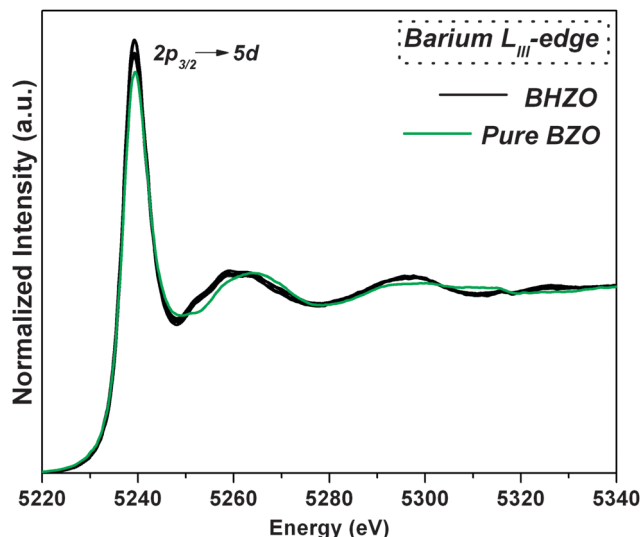

Fig. 9 Barium L$_{III}$-edge for pure and BHZO samples.
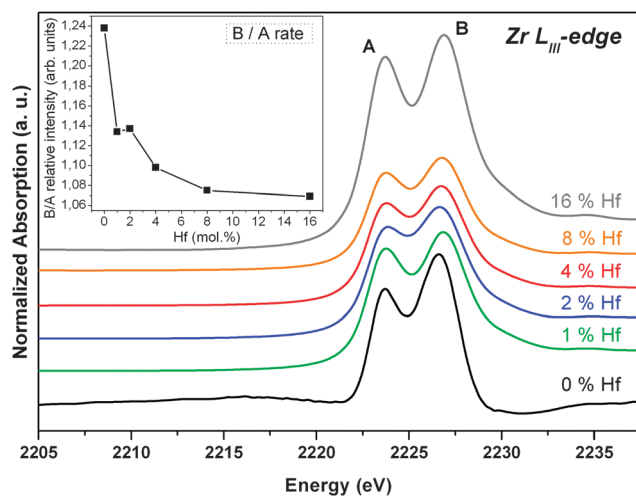

Fig. 8 Zirconium L$_{III}$-edge for peaks A and B reporting the e$_g$ and t$_{2g}$ contribution for L$_{III}$-edge. The inset denotes the B/A ratio.

10 were analysed in conjunction with the barium L$_{III}$-edge present in Fig. 9. In the zirconium K-edge significant changes are not easily observed, only by a subtle green line signal apparent in parts of the spectra, corresponding to the BZO undoped sample. Zr K-edge XANES spectra of crystalline BZO and BZHO compounds are depicted in Fig. 7. For BZO and BHZO systems, Zr is 6-coordinated to oxygen atoms into an octahedral cluster and the main edge is split into two well resolved features, "a" at 18 018.5 eV and "b" at 18 030.0 eV.[27] The more intense peak of the Zr K-edge match with the "b" feature. This assertion was confirmed by the XANES simulations performed by Giannici et al.,[43] taking into account two environments for Zr. Additionally at 40 eV after the "white line" (first absorption) a wide shoulder is evident, which is absent for ZrO$_2$ due to its tetrahedral environment. The existence of this supplementary shoulder is reported due to a strong Zr–Zr and/ or Zr–Ba correlation and subsequently multiple scattering for

octahedral environments is naturally expected for BZO and BZHO samples.[28]

The main distinguished "white lines" are evident for the zirconium L$_{III}$-edge, denoted by the intensity relationships between peaks "A" and "B" identified in Fig. 8. The height of the Zr L$_{III}$-edge feature has been shown to be related to the geometry of the Zr–oxygen polyhedra[44,45] and hence with its local distortions. Therefore, any change in the cluster environment alters the electronic structure of the absorbing atom and should be reflected in the corresponding optical properties results. The acquired spectra were measured at 25 °C, in which the cubic structure for BZO is the thermodynamically stable phase, even for high doped samples of 16% Hf. Although the cubic structure was maintained, the Hf 5d orbitals introduce a tendency of weak field support the increased typical d-splitting for Zr L$_{III}$-edge from 2.3 to 3.1 eV between the A and B peaks for the cubic BHZO local environment.[27] It is important to note that the 2.3 eV split is related to the tetrahedral crystal field. In our samples we have a octahedral crystal field, therefore the splitting increase as expected due to the crystal field theory to 3.1 eV. A careful analysis of Fig. 8 shows that the Zr L$_{III}$-edge of BZO is characterized by two main distinctive features, which correspond to a split between the signals of orbital levels xy, yz and xz for t$_{2g}$ and z^2, x^2 − y^2 for e$_g$ situated in the Zr edge represented by peaks A and B, respectively.[46] The separation of t$_{2g}$ and e$_g$ orbitals is related to crystal-field splitting effect denoted by electronic transitions from the occupied O 2p orbitals to the empty Zr 4d and/or Hf 5d orbitals as it was demonstrated in the theoretical modelling section. From the viewpoint of Zr local symmetry, all samples that have an octahedral crystal field symmetry (O$_h$ point group) report random disordered ZrO$_6$ octahedron into the cubic structure because the relative intensity between A and B peaks is different for each sample, most probably as a result of Hf presence.

For cubic systems the relative intensity between A and B peaks obeys the B/A rate higher than unity. The B/A relationship
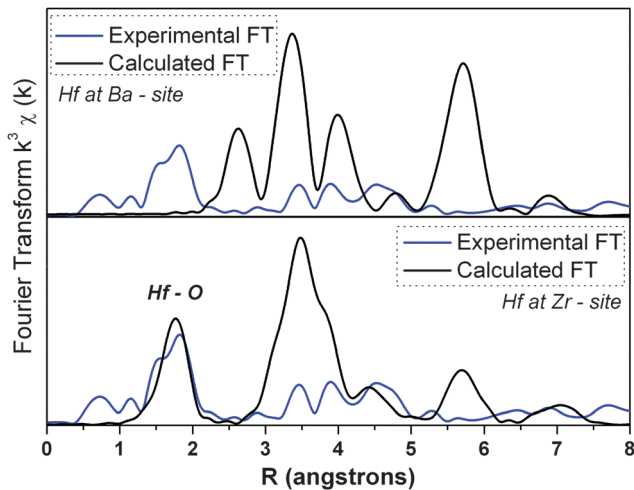
11346 | *Phys. Chem. Chem. Phys.*, 2015, **17**, 11341–11349

This journal is © the Owner Societies 2015

Fig. 10 Experimental and theoretical Fourier transformer of the first coordination sphere to identify the location of hafnium in the BZO host lattice. The simulation was performed for Hf substitution of Ba and Zr.

Fig. 11 FE-SEM images of decaoctahedral BZO and the surface smoothing for samples doped with hafnium.

for pure BZO and BZHO samples are displayed in the inset of Fig. 8. For Ba L_{III}-edge in Fig. 10 no difference can be sensed among BZHO doped samples, even under 16% Hf content in the BZO host lattice. On the other hand, for undoped samples there are significant variations in the XANES region. Then, it is mandatory to employ a more careful analysis of the Hf L_{III}-edge to determine the Hf replacements.

To this end, a comparison between experimental data and simulated EXAFS for 16% Hf replacement over Ba and Zr sites has been performed. EXAFS spectra were calculated by supposing the substitution of either Ba or Zr by Hf atoms in the Hf L_{III}-edge. Fig. 10 shows the Fourier Transform (FT) for each situation, the first FT peak corresponds to the first Hf–O coordination shell while the other peaks are related to further Hf-coordination shells.

As observed in Fig. 10, the simulated EXAFS spectrum for Hf oscillations located at Zr octahedral sites is quite similar to the experimental data, whereas the EXAFS spectrum of Hf at Ba cubooctahedral sites is completely different. Therefore, the Hf element is preferentially located in octahedral sites replacing Zr atom.

3.4 Microscopy and microanalysis

The scanning images provide information to evaluate the possible microscopic influence of the dopant content over shape and size of the samples. A detailed analysis of the results shows that the shape of decaoctahedral BZO was slightly affected by an increase of Hf amount. In Fig. 11 the smoothing effect of the decaoctahedral edge between adjacent facets is evident, *i.e.* a morphological change takes place, from a decaoctahedral shape to form a quasi-spherical assembled particle as the Hf content increases. We can also observe that the self-assembled process becomes more evident, probably due to the slight increase of individual nanoparticles. Recently, we have observed a reversed crystal growth process to pure BZO compound as a result of competition between self-assembly and Oswald ripening processes.[47] In this case the introduction of Hf seems to prevent Oswald repining, due to increased growth of individual grains
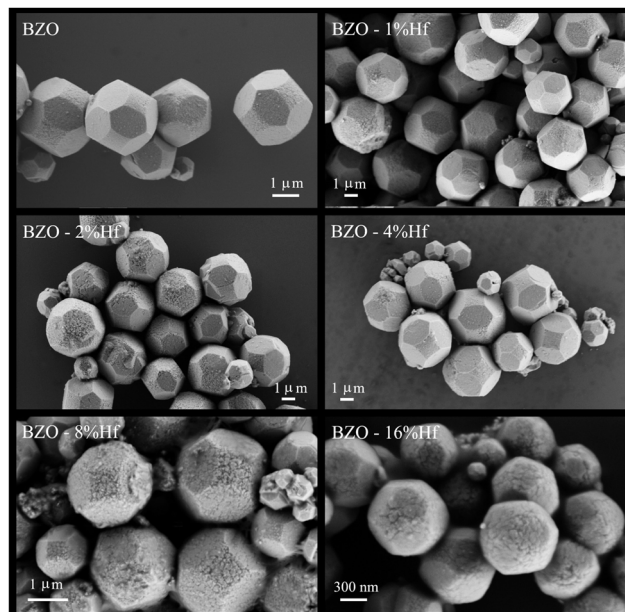
Table 2 FE-SEM Microanalysis for BZO and BHZO samples

Samples	Nominal hafnium content (%)	Microanalysis (%)
BZO	0	0
BHZO-1%	1	2.45
BHZO-2%	2	2.72
BHZO-4%	4	3.88
BHZO-8%	8	7.28
BHZO-16%	16	12.34

or/and by homogenization of the grain size distribution, avoiding a great reversed crystallization process as observed for pure BZO.[47]

One way to estimate the Hf content is microanalysis performed by FE-SEM. In Table 2 the Hf concentration proposed and results obtained from microanalysis are presented. An
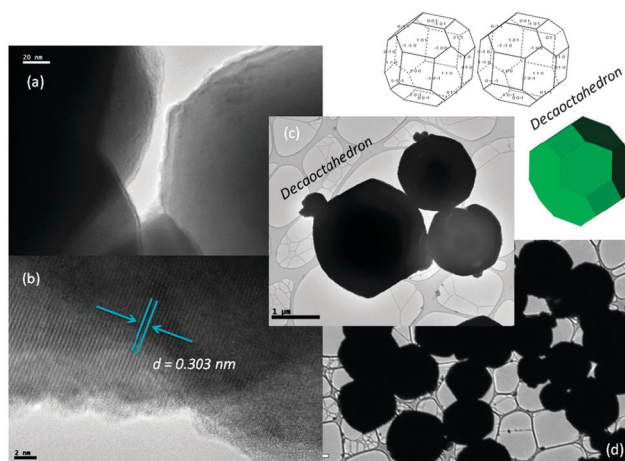

Fig. 12 Transmission electron microscopy of decaoctahedral BZO evidencing the typical *d*-spacing of BZO associated to the schematic model to surface (*hkl*) exposed.

analysis of these results allows us to conclude that the Hf was well included into the BZO host lattice for all concentrations until 8%, except 16%, which report only 12.5–13% of Hf. Then, this result allows us to use the largest concentration of Hf to carry out the simulations.

TEM reveals a mesocrystalline feature of the BHZO sample with 13% of Hf as indicated by microanalysis. It's important to note that the interplanar distance d = 0.303 nm was not changed if compared to the pure BZO lattice as can be seen in Fig. 12b. The decaoctahedral shape is still easily identified for same particles in the bright field image Fig. 12c for the BZHO sample with 16% Hf, however in Fig. 12d the majority of the particles have a spherical shape.

4 Conclusions

In summary, the main conclusions of the present work can be summarized as follows: (i) by means of the MAH method, we have successfully introduced Hf into the BaZrO$_3$ (BZO) host lattice to form a solid solution BaZr$_{1-x}$Hf$_x$O$_3$, x = 0.01, 0.02, 0.04, 0.08 and 0.16, BZHO. Hf^{4+} ions are successful introduced into the perovskite-type cubic structure to substitute for Zr^{4+} ions on the 6-fold coordination. (ii) The periodic structure, *i.e.* long-range structure was not strongly affected by the Hf introduction, while the local symmetry, *i.e.* short-range structure was modified and hence the electronic structure presents new behaviour. (iii) TEM analysis points out the mesocrystalline nature of the self-assembled BZHO nanoparticles under a decaoctahedral shape. (iv) XAS patterns are able to determine in which site Hf was introduced in the host lattice and assign short-range distortion on Zr–O and Hf–O bonds. (v) Band structures corroborate XAS results showing the split on states of the conduction band due to the 5d orbitals of hafnium. Density of states was used to observe a low contribution of 5d orbitals. However they are capable of introducing a split in the band structure. (vi) The introduction of the 5d states changes the polarization of the structure modifying the original Raman mode. These are confirmed by the good correlation found between simulated and experimental Raman results. (vii) These features can be use to interpret the electronic and optical properties of this system for luminescence emission at room temperature for crystalline perovskites.

Acknowledgements

References

1 J. Suntivich, H. A. Gasteiger, N. Yabuuchi, H. Nakanishi, J. B. Goodenough and Y. Shao-Horn, *Nat. Chem.*, 2011, **3**, 546–550.

2 Y. Zhao, L. Xu, L. Mai, C. Han, Q. An, X. Xu, X. Liu and Q. Zhang, *Proc. Natl. Acad. Sci. U. S. A.*, 2012, **109**, 19569–19574.

3 N. A. Benedek and C. J. Fennie, *J. Phys. Chem. C*, 2013, **117**, 13339–13349.

4 S. V. Bhide and A. V. Virkar, *J. Electrochem. Soc.*, 1999, **146**, 4386–4392.

5 I. Antunes, G. Mather, J. Frade, J. Gracio and D. Fagg, *J. Solid State Chem.*, 2010, **183**, 2826–2834.

6 L. Cavalcante, V. Longo, M. Zampieri, J. Espinosa, P. Pizani, J. Sambrano, J. Varela, E. Longo, M. Simoes and C. Paskocimas, *J. Appl. Phys.*, 2008, **103**, 063527.

7 M. L. Moreira, J. Andrés, J. A. Varela and E. Longo, *Cryst. Growth Des.*, 2009, **9**, 833–839.

8 R. Borja-Urby, L. Diaz-Torres, P. Salas, M. Vega-Gonzalez and C. Angeles-Chavez, *Mater. Sci. Eng., B*, 2010, **174**, 169–173.

9 Z. Lu, Y. Tang, L. Chen and Y. Li, *J. Cryst. Growth*, 2004, **266**, 539–544.

10 G. Łupina, J. Dabrowski, P. Dudek, G. Kozłowski, P. Zaumseil, G. Lippert, O. Fursenko, J. Bauer, C. Baristiran and I. Costina, *et al.*, *Appl. Phys. Lett.*, 2009, **94**, 152903.

11 H. Huhtinen, K. Schlesier and P. Paturi, *Supercond. Sci. Technol.*, 2009, **22**, 075019.

12 S. H. Wee, E. D. Specht, C. Cantoni, Y. L. Zuev, V. Maroni, W. Wong-Ng, G. Liu, T. J. Haugan and A. Goyal, *Phys. Rev. B: Condens. Matter Mater. Phys.*, 2011, **83**, 224520.

13 R. Borja-Urby, L. Dáz-Torres, P. Salas, E. Moctezuma, M. Vega and C. Ángeles-Chávez, *Mater. Sci. Eng., B*, 2011, **176**, 1382–1387.

14 M. L. Moreira, D. P. Volanti, J. Andrés, P. J. Montes, M. E. Valerio, J. A. Varela and E. Longo, *Scr. Mater.*, 2011, **64**, 118–121.

15 T. M. Mazzo, M. L. Moreira, I. M. Pinatti, F. C. Picon, E. R. Leite, I. L. Rosa, J. A. Varela, L. A. Perazolli and E. Longo, *Opt. Mater.*, 2010, **32**, 990–997.

16 Y. Inaguma, T. Muronoi, K. Sano, T. Tsuchiya, Y. Mori, T. Katsumata and D. Mori, *Inorg. Chem.*, 2011, **50**, 5389–5395.

17 I. Bilecka and M. Niederberger, *Nanoscale*, 2010, **2**, 1358–1374.

18 A. Ristić, K. Lázár, H. Solt and V. Kaucic, *CrystEngComm*, 2011, **13**, 1946–1952.

19 N. Shojaee, T. Ebadzadeh and A. Aghaei, *Mater. Charact.*, 2010, **61**, 1418–1423.

20 X. Wang, K. Qu, B. Xu, J. Ren and X. Qu, *J. Mater. Chem.*, 2011, **21**, 2445–2450.

21 H. J. Kitchen, S. R. Vallance, J. L. Kennedy, N. Tapia-Ruiz, L. Carassiti, A. Harrison, A. G. Whittaker, T. D. Drysdale, S. W. Kingman and D. H. Gregory, *Chem. Rev.*, 2014, **114**, 1170–1206.

22 G. J. Wilson, A. S. Matijasevich, D. R. Mitchell, J. C. Schulz and G. D. Will, *Langmuir*, 2006, **22**, 2016–2027.

11348 | *Phys. Chem. Chem. Phys.*, 2015, **17**, 11341–11349

This journal is © the Owner Societies 2015

23 H. Katsuki, S. Furuta and S. Komarneni, *J. Porous Mater.*, 2001, **8**, 5–12.

24 M. A. Herrero, J. M. Kremsner and C. O. Kappe, *J. Org. Chem.*, 2008, **73**, 36–47.

25 W. C. Conner and G. A. Tompsett, *J. Phys. Chem. B*, 2008, **112**, 2110–2118.

26 F. Giannici, M. Shirpour, A. Longo, A. Martorana, R. Merkle and J. Maier, *Chem. Mater.*, 2011, **23**, 2994–3002.

27 L. Galoisy, E. Pélegrin, M.-A. Arrio, P. Ildefonse, G. Calas, D. Ghaleb, C. Fillet and F. Pacaud, *J. Am. Ceram. Soc.*, 1999, **82**, 2219–2224.

28 G. Mountjoy, D. M. Pickup, R. Anderson, G. W. Wallidge, M. A. Holland, R. J. Newport and M. E. Smith, *Phys. Chem. Chem. Phys.*, 2000, **2**, 2455–2460.

29 J. P. Ko, Y.-M. Yiu, H. Liang and T.-K. Sham, *J. Chem. Phys.*, 2010, **132**, 234701.

30 D. Andrault and J. Poirier, *Phys. Chem. Miner.*, 1991, **18**, 91–105.

31 P. Dobal, A. Dixit, R. Katiyar, Z. Yu, R. Guo and A. Bhalla, *J. Appl. Phys.*, 2001, **89**, 8085–8091.

32 A. D. Becke, *Phys. Rev. A*, 1988, **38**, 3098.

33 E. Longo, E. Orhan, F. Pontes, C. Pinheiro, E. Leite, J. Varela, P. Pizani, T. Boschi, F. Lanciotti Jr and A. Beltran, *et al*, *Phys. Rev. B: Condens. Matter Mater. Phys.*, 2004, **69**, 125115.

34 A. D. Becke, *J. Chem. Phys.*, 1993, **98**, 5648–5652.

35 V. M. Longo, L. S. Cavalcante, M. G. Costa, M. L. Moreira, A. T. de Figueiredo, J. Andrés, J. A. Varela and E. Longo, *Theor. Chem. Acc.*, 2009, **124**, 385–394.

36 M. L. Moreira, P. G. C. Buzolin, V. M. Longo, N. H. Nicoleti, J. R. Sambrano, M. S. Li, J. A. Varela and E. Longo, *J. Phys. Chem. A*, 2011, **115**, 4482–4490.

37 V. R. S. Dosevi, *CRYSTAL06 user's manual*, University of Torino, Torino, 2006.

38 R. Evarestov and V. Smirnov, *J. Phys.: Condens. Matter*, 1997, **9**, 3023.

39 R. Loudon, *Adv. Phys.*, 1964, **13**, 423–482.

40 K. Dhahri, M. Bejar, E. Dhahri, M. Soares, M. Graça, M. Sousa and M. Valente, *Chem. Phys. Lett.*, 2014, **610–611**, 341–344.

41 H. Yamashita, S. Yamaguchi, M. Yokozeki, M. Nakashima and T. Maekawa, *Nippon Seramikkusu Kyokai Gakujutsu Ronbunshi*, 1999, **107**, 895–900.

42 A. Bouhemadou, F. Djabi and R. Khenata, *Phys. Lett. A*, 2008, **372**, 4527–4531.

43 F. Giannici, A. Longo, A. Balerna, K.-D. Kreuer and A. Martorana, *Chem. Mater.*, 2009, **21**, 2641–2649.

44 N. Thromat, C. Noguera, M. Gautier, F. Jollet and J. Duraud, *Phys. Rev. B: Condens. Matter Mater. Phys.*, 1991, **44**, 7904.

45 J. A. Rodriguez, J. C. Hanson, J.-Y. Kim, G. Liu, A. Iglesias-Juez and M. Fernández-Garcá, *J. Phys. Chem. B*, 2003, **107**, 3535–3543.

46 F. Zhang, P. J. Chupas, S. L. A. Lui, J. C. Hanson, W. A. Caliebe, P. L. Lee and S.-W. Chan, *Chem. Mater.*, 2007, **19**, 3118–3126.

47 M. L. Moreira, J. Andrés, V. R. Mastelaro, J. A. Varela and E. Longo, *CrystEngComm*, 2011, **13**, 5818–5824.